PHYSICAL REVIEW E VOLUME 61, NUMBER 1 JANUARY 2000

Proper orthogonal decomposition and Galerkin projection for a three-dimensional plasma dynamical system

P. Beyer and S. Benkadda
Equipe Dynamique des Systèmes Complexes, LPIIM, CNRS–Université de Provence, Centre de St. Jérôme, Case 321, 13397 Marseille Cedex 20, France

X. Garbet
Association Euratom–CEA sur la Fusion,CEA Cadarache, 13108 St.-Paul-lez-Durance, France

(Received 15 March 1999; revised manuscript received 27 September 1999)

A general method by which to investigate nonlinear dynamical systems close to a stability threshold is presented. This method combines a proper orthogonal decomposition and a subsequent Galerkin projection. This technique is applied to three-dimensional resistive ballooning plasma fluctuations in a tokamak. The corresponding dynamical system belongs to a large family of convective fluid systems including Rayleigh-Bénard convection. A proper orthogonal decomposition of the fluctuating signal obtained by numerical simulation shows that the relevant modes are close to the linear (global) modes. The Galerkin projection provides a low-dimensional system that allows the study of shear flow generation, its subsequent fluctuation reduction, and the evolution to oscillating states.

PACS number(s): 52.35.Ra, 52.35.Py, 47.27.Eq, 52.35.Mw

I. INTRODUCTION

Nonlinear dynamical systems close to a stability threshold are often investigated through reduced sets of ordinary differential equations (ODE's). Such a reduced system indeed provides information on the possible bifurcations. These equations are generally obtained by a Galerkin approximation, i.e., by projecting the original equations onto a set of basis functions. However, the best choice of basis functions is not always obvious. Even if the set of linear eigenmodes seems to be a natural choice, the number of functions that have to be kept is not a trivial matter. Here, we propose a numerical method using a proper orthogonal decomposition (POD) [1,2]. This method is appropriate when full numerical simulations (or experimental measurements) of the dynamical system exist. A POD analysis provides a set of eigenvalues and associated space- and time-dependent eigenfunctions. The spectrum of eigenvalues is used to determine the accuracy in the cutoff and the space-dependent eigenfunctions are used for the Galerkin projection.

The method is illustrated by studing a three-dimensional (3D) resistive ballooning plasma fluctuations in a tokamak. The model describes a convective dynamics and belongs to a large family of fluid systems including Rayleigh-Bénard convection [3]. Numerical simulations show that two possible steady-states exist close to the instability threshold. One state corresponds to a finite level of fluctuations and no global flow. The second state is characterized by a reduced fluctuation level and a self-generated sheared flow. The dynamics involving these two states has been already analyzed elsewhere and it has been proposed as a paradigm for the L (low confinement) to H (high confinement) transition in a tokamak [4,5]. In a more unstable situation, oscillating states are also observed. Performing a POD analysis of these numerical simulations, it turns out that *the dynamics is dominated by five modes* and that *these modes are close to the linear eigenmodes*.

The latter point is not trivial in the sense that linear eigenmodes are not simple in tokamaks. The determination of these modes, called ''global modes'' [6–8], is part of this work. Projecting the 3D nonlinear equations onto this set of eigenmodes, a reduced system of five ODE's is found. Distinguishing between main and slaved modes, the system can be further reduced to three ODE's. This system is characterized by two nontrivial fixed points, which correspond to the L and H state mentioned above. The stability of these fixed points, which depends on the normalized dissipation and the evolution to a limit cycle representing an oscillating state, agrees well with the results of the simulations.

The remainder of the paper is organized as follows. In the second section, we present the physical model, the linear stability properties of the corresponding dynamical system, and the numerical simulations in the nonlinear regime. The third section is dedicated to the POD analysis, the construction and the discussion of the low-dimensional model. Conclusions are presented in the fourth section.

II. NUMERICAL SIMULATIONS

A. Model

For the simulation of plasma fluctuations in a tokamak, we use a reduced magnetohydrodynamical (MHD) model that follows from the resistive MHD equations taking into account that fluctuations are nearly aligned along magnetic field lines (flute approximation $k_\parallel \ll k_\perp$) [9]. The model describes resistive ballooning fluctuations, and, for small plasma pressure ($p \ll B^2/2\mu_0$) and small inverse aspect ratio ($a/R \ll 1$), it consists of two field equations for the vorticity and pressure fluctuations. The normalized form of these equations is

$$\frac{d}{dt}\nabla_\perp^2 \phi = -\nabla_\parallel^2 \phi - Gp + \nu \nabla_\perp^4 \phi, \tag{1}$$

1063-651X/2000/61(1)/813(11)/$15.00

$$\frac{dp}{dt} = -\frac{\partial \phi}{\partial y} + \chi_\parallel \nabla_\parallel^2 p + \chi_\perp \nabla_\perp^2 p. \tag{2}$$

Here, $d/dt = \partial/\partial t + \{\phi, \cdot\}$, where the Poisson bracket represents the convection due to the dominant $\vec{E}\times\vec{B}$ flow; the normalized electrostatic potential ϕ represents a flux function of the flow. In this MHD model, diamagnetic effects and magnetic fluctuations are not implemented. Of course, for a complete simulation of plasma turbulence in a tokamak, more sophisticated models have to be used [10,11]. However, the present simplified model allows the understanding of basic dynamic processes at the plasma edge. Note that this is a convective model close to other systems used in fluid dynamics, e.g., in 2D (i.e., $\nabla_\parallel = 0$), Eqs. (1) and (2) are exactly those for Rayleigh-Bénard convection where G is proportional to the gravity [3]. The 2D version has also been investigated in [9] using a center manifold approach.

The magnetic field in toroidal coordinates is $\vec{B}_0 = B_\varphi[\hat{e}_\varphi + r/(Rq)\hat{e}_\theta]$. For the purposes of implementation, normalized slab coordinates are introduced in the vicinity of a reference surface $r = r_0$,

$$x = \frac{r - r_0}{\xi}, \quad y = \frac{r_0 \theta}{\xi}, \quad z = \frac{R_0 \varphi}{L_s},$$

where the perpendicular length scale ξ is typically a few ion Larmor radii and the shear length L_s is of the order of R_0. Time is normalized to the interchange time. ν, $\chi_\parallel$, $\chi_\perp$ are the normalized viscosity, parallel and perpendicular heat conductivity, respectively. A detailed description of the normalization is given in [12].

For the safety factor $q(r)$ a linear approximation of $1/q$ is used and the resulting normalized parallel gradient is given by

$$\nabla_\parallel = \frac{\partial}{\partial z} + \left(\frac{\kappa_z}{\kappa_y q_0} - x\right)\frac{\partial}{\partial y}$$

where $\kappa_y = \xi/r_0$ and $\kappa_z = L_s/r_0$.

The ballooning instability is driven on the low field side by the combination of the pressure gradient and the toroidal curvature of the field lines. The latter emerges from the operator

$$G = \sin(\kappa_y y)\frac{\partial}{\partial x} + \cos(\kappa_y y)\frac{\partial}{\partial y}.$$

As we will see below, the instability presents a threshold. In our simulations, we fix $\chi_\parallel$ and use $\chi_\perp = \nu$ as a control parameter. Note that due to our normalization, this parameter is proportional to the mean pressure gradient length.

The variables ϕ, p are expanded in a Fourier-mode representation in the poloidal and toroidal directions,

$$\begin{pmatrix}\phi\\ p\end{pmatrix} = \sum_{m,n}\begin{pmatrix}\phi_{mn}(x,t)\\ p_{mn}(x,t)\end{pmatrix}\exp(im\kappa_y y - in\kappa_z z).$$

B. Linear stability

1. Analytic calculation of ballooning modes

The toroidal curvature of field lines causes harmonics (m,n) to couple linearly to their neighbors $(m\pm 1,n)$ and to form global modes that have a large radial extent. In the high toroidal wave-number limit $(n \gg 1)$, the growth rate and the radial envelope of such modes can be calculated analytically in the ballooning approximation. For each toroidal mode number $n =: 1/\epsilon$, the main harmonic $(nq_0,n) =: (m_0,n)$ is separated,

$$\Phi = \hat{\Phi}(x,y)\exp(im_0\kappa_y y - in\kappa_z z + \gamma t), \tag{3}$$

where $\Phi = (-i\phi, p)$ and the amplitude varies only slowly in the poloidal direction relative to the main harmonic, i.e., $|\partial\hat{\Phi}/\partial y|/|m_0\kappa_y\hat{\Phi}| \sim \epsilon$. Equations (1) and (2) are linearized and a Fourier transformation

$$\hat{\Phi}(x,y) = \frac{1}{\sqrt{2\pi}}\int_{-\infty}^{\infty} dk_x \Phi(k_x,y)\exp(ik_x x) \tag{4}$$

is applied in the radial direction. Following the presentation in [6–8], a subsequent coordinate transformation

$$\theta' = \theta = \kappa_y y, \quad k_x' = k_x - \frac{\kappa_y y}{d_0}, \tag{5}$$

is performed. If only the dominant (ϵ^0) terms are kept, this leads to the eigenvalue problem

$$\gamma\Phi = \tilde{\mathbf{L}}_0(\theta', \theta_0)\Phi, \tag{6}$$

where

$$\tilde{\mathbf{L}}_0 = \frac{1}{s_0^2}\begin{pmatrix}\frac{1}{k_\perp^2} & 0\\ 0 & \chi_\parallel\end{pmatrix}\frac{\partial^2}{\partial\theta'^2} + \begin{pmatrix}-\nu k_\perp^2 & \frac{m_0\kappa_y g}{k_\perp^2}\\ m_0\kappa_y & -\chi_\perp k_\perp^2\end{pmatrix}$$

and

$$k_\perp^2(\theta', \theta_0) = \frac{(\theta' - \theta_0)^2}{d_0^2} + (m_0\kappa_y)^2,$$

$$g(\theta', \theta_0) = \cos(\theta') + (\theta' - \theta_0)s_0\sin(\theta').$$

$s_0 = q_0/\kappa_z$ is the shear and $d_0 = 1/(m_0\kappa_y s_0)$ is the normalized distance between resonant surfaces. The problem has essentially been reduced now to one dimension with the variable $\theta_0 = -d_0 k_x'$ as a parameter which is called the ballooning angle. Obviously, the growth rate γ is periodic in θ_0 and turns out to be maximal at $\theta_0 = 0, \pm 2\pi, \pm 4\pi, \ldots$. The dependence of this maximal value of γ on the poloidal wave number m_0 is shown in Fig. 1 for two sets of parameters.

For each eigenvalue $\gamma(\theta_0)$, the problem (6) is solved by an infinite set of eigenfunctions $\tilde{\Phi}[\theta', \theta_0 + 2\pi l] = \tilde{\Phi}[\theta' - 2\pi l, \theta_0]$. Therefore, the most unstable periodic (in $\theta' = \theta$) solution of the linear problem to lowest order can be constructed in the following way:

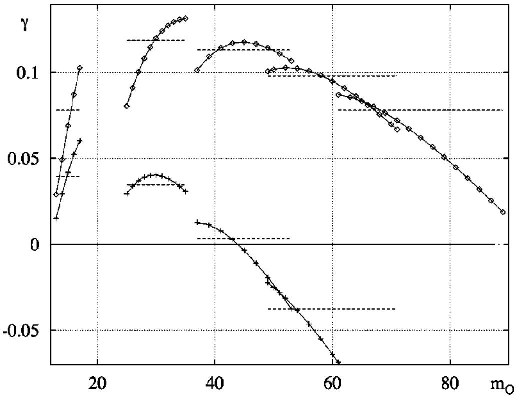

FIG. 1. Linear growth rates of (m_0,n) modes in the lowest order ballooning approximation for $\chi_\parallel=1$, $\nu=\chi_\perp=2$ (boxes), and $\nu=\chi_\perp=4$ (crosses). Dashed lines indicate the growth rates of the corresponding $n=6,12,18,24,30$ ballooning modes obtained by a numerical resolution of the complete eigenvalue problem.

$$\Phi(\theta',\theta_0)=\delta(\theta_0)\sum_{l=-\infty}^{\infty}\tilde{\Phi}(\theta'-2\pi l,\theta_0).$$

The back-transformation of Eqs. (3)–(5) results for $y\in[-\pi/\kappa_y;\pi/\kappa_y]$,

$$\Phi=\frac{1}{\sqrt{2\pi}d_0}\tilde{\Phi}(\kappa_y y,0)\exp\left[i\kappa_y\left(m_0+\frac{x}{d_0}\right)y-in\kappa_z z+\gamma(0)t\right].$$

This solution can be written in a Fourier series,

$$\Phi=\frac{1}{2\pi d_0}\sum_{\mu}\mathcal{F}\tilde{\Phi}\left(\frac{x}{d_0}-\mu\right)\exp[i(m_0+\mu)\kappa_y y-in\kappa_z z+\gamma(0)t],\qquad(7)$$

where the radial structure of each Fourier mode is described by the Fourier transformation of the eigenfunction $\tilde{\Phi}(\kappa_y y,0)$, which is typically Gaussian-shaped. However, the global mode (7) is not localized in the radial direction, i.e., all Fourier modes have the same amplitude. To capture the localization of the mode, one additional order must be retained in the ballooning approximation.

The eigenvalue problem up to the order ϵ^2 can be written in the form

$$[\mathbf{L}_0(\gamma,\theta',\theta_0)+i\epsilon\mathbf{L}_1(\gamma,\theta',\theta_0)+\epsilon^2\mathbf{L}_2(\gamma,\theta',\theta_0)]\Phi=0,\qquad(8)$$

where the smallness parameter ϵ has been formally introduced. Developing the lowest order operator $\mathbf{L}_0(\gamma,\theta',\theta_0):=\tilde{\mathbf{L}}_0-\gamma$, the solution $\tilde{\Phi}(\theta',\theta_0)$, and the growth rate $\gamma_0(\theta_0)$ around $\theta_0=0$ with $\theta_0=O(\epsilon^{1/2})$, a solution of the two-dimensional eigenvalue problem (8) in the vicinity of $\tilde{\Phi}_0(\theta',\theta_0)$ and $\gamma_0(0)$ can be constructed. The detailed calculation is presented in the Appendix. The result is

$$\Phi=\frac{1}{\sqrt{2\pi\alpha}d_0}\sum_{\mu}\exp\left(-\frac{x^2}{2\alpha d_0^2}\right)\mathcal{F}\tilde{\Phi}_0\left(\frac{x}{d_0}-\mu\right)\times\exp[i\kappa_y(m_0+\mu)y-in\kappa_z z+(\gamma_0(0)+\gamma_2)t].\qquad(9)$$

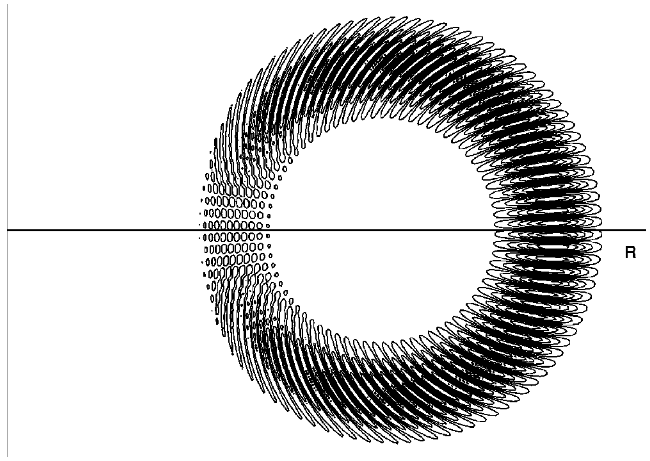

FIG. 2. Contour plot of the potential ϕ of a $n=18$ ballooning mode radially localized in the region $x\in[x_{q=2};x_{q=3}]$ in the poloidal plane $z=0$. (The vertical axis on the left represents the main axis of the torus.) Here, $\nu=\chi_\perp=2$.

As for the solution in zeroth order (7), the radial structure of each Fourier component is characterized by the Fourier transformation of the function $\tilde{\Phi}_0(\kappa_y y,0)$. However, in (9), a slowly varying envelope is superimposed which captures the radial localization of the mode.

A linear eigenmode is therefore a combination of several Fourier modes with the same toroidal wave number *n* and different poloidal wave numbers *m*. It has a much broader radial profile than one single Fourier mode. These are the characteristics of the so-called global modes.

2. Numerical computation of global modes

As we can see from Fig. 1, the most unstable resistive ballooning modes are those with low toroidal wave numbers *n*. For these modes, we do not expect the first order ballooning approximation to give quantitativly good results, and we therefore solve the eigenvalue problem numerically. The resulting maximal growth rates are given in Fig. 1. In Fig. 2, we show a contour plot in a poloidal plane of the potential ϕ for a typical eigenmode. Because the toroidal curvature is unfavorable on the low field side of a torus, the mode amplitudes are much larger in this region relative to the high field side. This is why these modes are called ''ballooning'' modes.

In order to present the radial structure of such a mode with a given toroidal wave number *n*, we plot the radial profiles of the different Fourier modes involved with $m=2n\ldots3n$ in one graph. For a typical case, the result is plotted in Figs. 3(a) and 3(b) for the most unstable and the second most unstable mode, respectively. The corresponding growth rates are $\gamma_1=2.9\times10^{-2}$ and $\gamma_{\overline{1}}=-4.6\times10^{-3}$, respectively. For the first mode, each Fourier component has a narrow profile which is approximately Gaussian and is localized at one radial position given by the resonance condition $q(x)=m/n$. The amplitudes of the different Fourier modes are determined by a broad radial envelope which is also approximately Gaussian. This structure is qualitatively well described by the analytical expression (9). The second most unstable mode has an odd envelope profile, which can be analytically approximated by the second unstable solution of

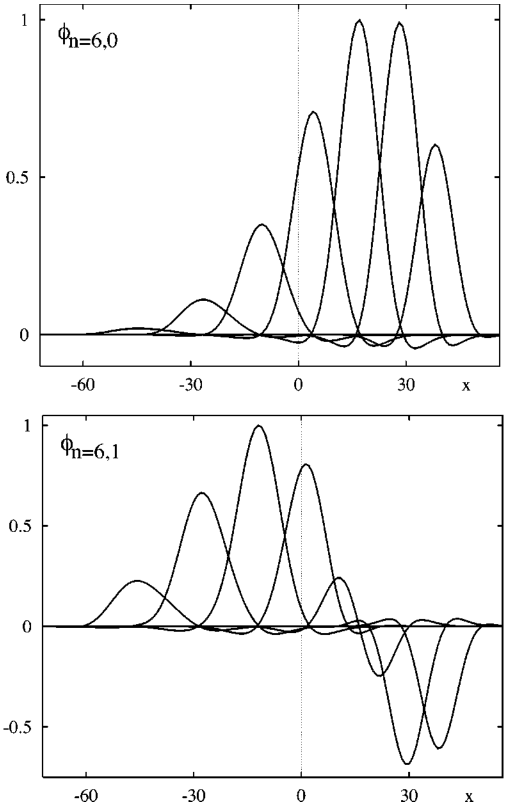

FIG. 3. Radial profiles of Fourier modes involved in the real part of the potential of the most unstable ($\phi_{n=6,0}$) and second most unstable ($\phi_{n=6,1}$) $n=6$ ballooning modes for $\chi_{\|}=2$, $\nu=\chi_{\perp}=3.5$.

Eq. (A3). Note that the Fourier mode localized near the knot of the envelope function also has an odd profile that can be described by a second unstable solution of the zeroth order problem (6).

C. Simulations in the nonlinear regime

We now have identified the structure of the linear global modes characterized by a coupling of several Fourier modes over a broad radial domain. The fundamental question that naturally arises is the role of these modes in the presence of nonlinear coupling. We will address this question in the next chapter. First, we will describe the important nonlinear phenomenon of shear flow generation captured by our model.

Each Fourier mode is localized at a resonant surface $q=m/n$ determined by a vanishing parallel gradient. Since we want to study the interaction of ballooning modes at the plasma edge, the simulation region is restricted to the domain between the $q=2$ and $q=3$ surfaces. Only those modes that are resonant in this interval are considered, up to toroidal mode number $n=30$. In order to restrict the number of modes we have to deal with in the 3D simulations, we only include toroidal mode numbers of $n=0,6,12,18,\ldots$ in the code. This does not represent an essential restriction because due to the axisymmetry of the geometry, there is no linear coupling between modes with different toroidal wave numbers. The nonlinear coupling is resolved by taking into account all modes with a given difference in toroidal wave number ($\Delta n=6$). In the radial direction, finite differences are used and all fluctuations are extrapolated to zero at a width Δ outside the interval $[x_{q=2};x_{q=3}]$.

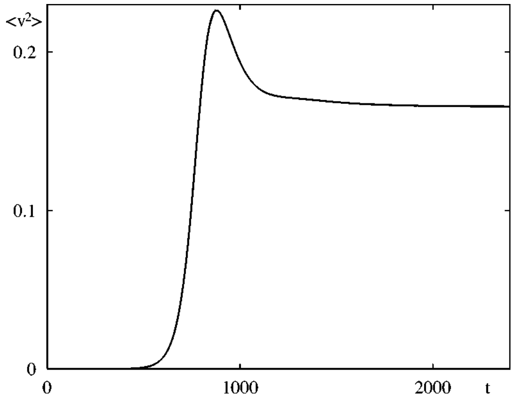

FIG. 4. Time evolution of the volume-averaged kinetic energy of the fluctuations close to the onset of instability ($\nu=\chi_{\perp}=4.5$).

The aspect of local flattening of the mean pressure gradient due to turbulence and its implications regarding transport dynamics is not discussed here. Therefore, the retroaction of the electrostatic fluctuations on the pressure profile are excluded in the simulations. This is done by neglecting the nonlinear term in the evolution equation of p_{00}. Further investigations show that by removing this constraint and by driving the instability by a constant flux, an intermittent transport with bursts can be observed in the 3D simulations [13], similarly to the results presented in Ref. [14] for 2D interchange turbulence.

As usual, starting with some small-amplitude white noise, the numerical simulations show an exponential growth of potential and pressure fluctuations and the achievement of a nonlinear saturated state. In a case close to the onset of instability, this behavior is illustrated in Fig. 4, where the volume-averaged kinetic energy of the fluctuations $v^2=(\partial_x\phi)^2+(\partial_y\phi)^2$ is plotted versus time. Note that in this case, a contribution of the $(m,n)=(0,0)$ component associated with an equilibrium electric field and an equilibrium velocity of the plasma is not observed.

This situation changes when we lower the control parameter going to a more unstable case. Now, as illustrated in Fig. 5, a significant contribution of a $(m,n)=(0,0)$ component develops. In the velocity field $\vec{v}=\hat{e}_z\times\nabla\phi$, this component corresponds to a sheared poloidal rotation

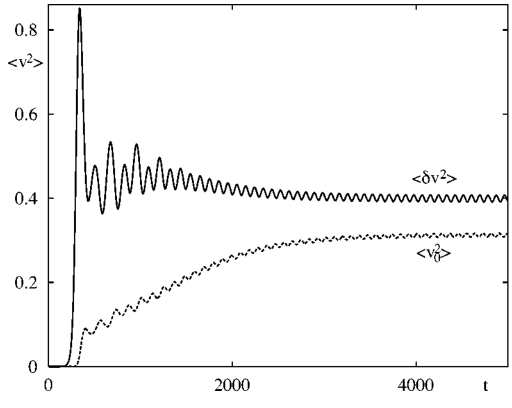

FIG. 5. Same as Fig. 4, in a more unstable case ($\nu=\chi_{\perp}=3.5$).

$$v_0(x,t)=\frac{\partial}{\partial x}\phi_{00}(x,t) \tag{10}$$

of the plasma. Because the $(m,n)=(0,0)$ mode is linearly stable, the generation of shear flow must be a nonlinear phenomenon. In the following, we will address the question of the relevant modes in this process and we will analyze their mechanism of interaction leading to the self-generation of poloidal rotation by the fluctuations. Note that in the presence of the shear flow, the level of turbulence is reduced. A simulation in which the $(m,n)=(0,0)$ component is artificially suppressed leads to a 28% higher fluctuation level for the same parameters.

III. LOW-DIMENSIONAL MODEL

A. Proper orthogonal decomposition

In order to identify the structures relevant in the process of shear flow generation, we apply the proper orthogonal decomposition (POD) method [1,15] to a time series obtained from the numerical simulation illustrated in Fig. 5. Therefore, the real part of the Fourier components of the potential $\mathrm{Re}\phi_{mn}(x_i,t_j)$ is sampled at subsequent times $t_1,\ldots,t_N$ and the data is assembled in a $N\times M$ matrix Φ^R_{jk}, where $k=1\ldots M$ covers all spatial indices (m,n,i). M is given by the number of Fourier modes times the number of radial grid points.

The POD consists in expanding the discrete data into a unique set of modes that are orthonormal in time and space,

$$\Phi^R_{jk}=\sum_{l=0}^{L-1} w_l A_l(t_j) F_l[(m,n,i)_k],$$

where $L=\min(N,M)$. The base functions $A_l(t_j)$ and $F_l[(m,n,i)_k]$ are eigensolutions of the two-point temporal and spatial cross correlation matrices, respectively [15]. The series is sorted in decreasing weight (w_l) order. Coherent structures that are highly correlated in time or in space appear in heavily weighted components.

Evaluating the contributions of the different Fourier modes in the simulation, we see that only a fraction of 10^{-4} of the total energy is contained in the modes with toroidal wave number $n>18$. In the POD, we therefore consider only Fourier modes up to $n=18$, which gives a total number of 3360 sampling points in the spatial direction (40 Fourier modes times 84 radial grid points). In the time direction, the signal is sampled at 500 points in the saturated state shown in Fig. 5 from $t=4000$ to $t=5000$. The values of the first 50 weights are plotted in Fig. 6 on a logarithmic scale. Apparently, the importance of the modes decreases rapidly with increasing weight order.

The temporal behavior of the first four modes is shown in Fig. 7. The first mode $(l=0)$ has a nearly constant amplitude. Some very small oscillations around the mean value reproduce the oscillations observed in the saturation (Fig. 5). We therefore associate this first mode with the equilibrium part of the signal. This identification is also supported by the spatial structure of the mode that is completely dominated by the $(m,n)=(0,0)$ part. The amplitudes of the radial profiles of all contributions with (m,n) different from zero are less than 1% of those of the equilibrium part. The latter is shown in Fig. 8. Obviously, the radial profile has a minimum near $x=0$. Therefore, the corresponding flow (10) is in opposite directions at the inner and outer regions of our simulation domain (sheared flow).

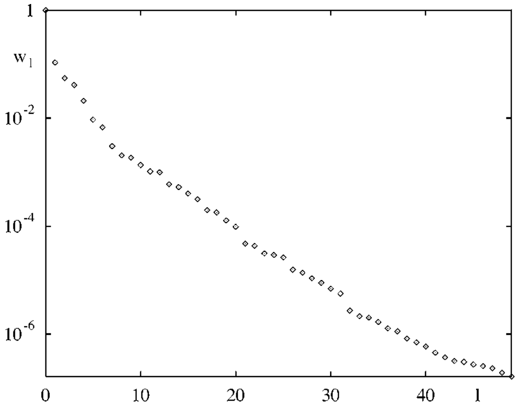

FIG. 6. First weights of the POD.

As can be seen in Fig. 7(b), the second important mode $(l=1)$ oscillates periodically in time. Its spatial structure is dominated by the $n=6$ parts; each contribution with toroidal wave number different from 6 is less than 4%. In order to present the structure of this mode, we plot the radial profiles of the contributions of the different Fourier modes with $n=6$ and $m=2n\ldots3n$ in one graph. The result is shown in Fig. 9. It strongly resembles the linear eigenmode presented in Fig. 3(a).

The third and fourth important modes in the POD $(l=2,3)$ show a quasiperiodic behavior in time [Figs. 7(c) and 7(d)]. Their spatial structures are dominated by combinations of $n=6$ and $n=12$ parts shown in Fig. 10 for $l=2$ and Fig. 11 for $l=3$. Each other contribution is less than 0.6% in amplitude. Here, the $n=6$ parts strongly resemble the second unstable global mode presented in Fig. 3(b). The $n=12$ parts are also governed by the corresponding global modes.

We therefore conclude that the modes relevant in the process of shear flow generation revealed by the POD of our nonlinear simulations are determined by the linear global modes. Especially, we identify the five most important modes, which are the most unstable global modes with $n=0,6,12$ (labeled by the indices 0, 1, and 2, respectively, below) and the second most unstable global modes with $n=6,12$ (labeled $\overline{1}$ and $\overline{2}$, respectively). In spite of analyzing a situation close to the threshold of instability, this is not an obvious result, because the linear global modes are large scale structures which we expect to be sensitive to the nonlinear coupling.

B. Galerkin projection

The preceding analysis indicates that the system can be described by a low-dimensional model. We will now construct such a model for the dynamics of the amplitudes of the relevant modes that we have identified in the last section. This low dimensional system should describe the mechanisms of interaction of these modes in the process of shear flow generation and fluctuation reduction.

The evolution equations (1,2) can be written in the form

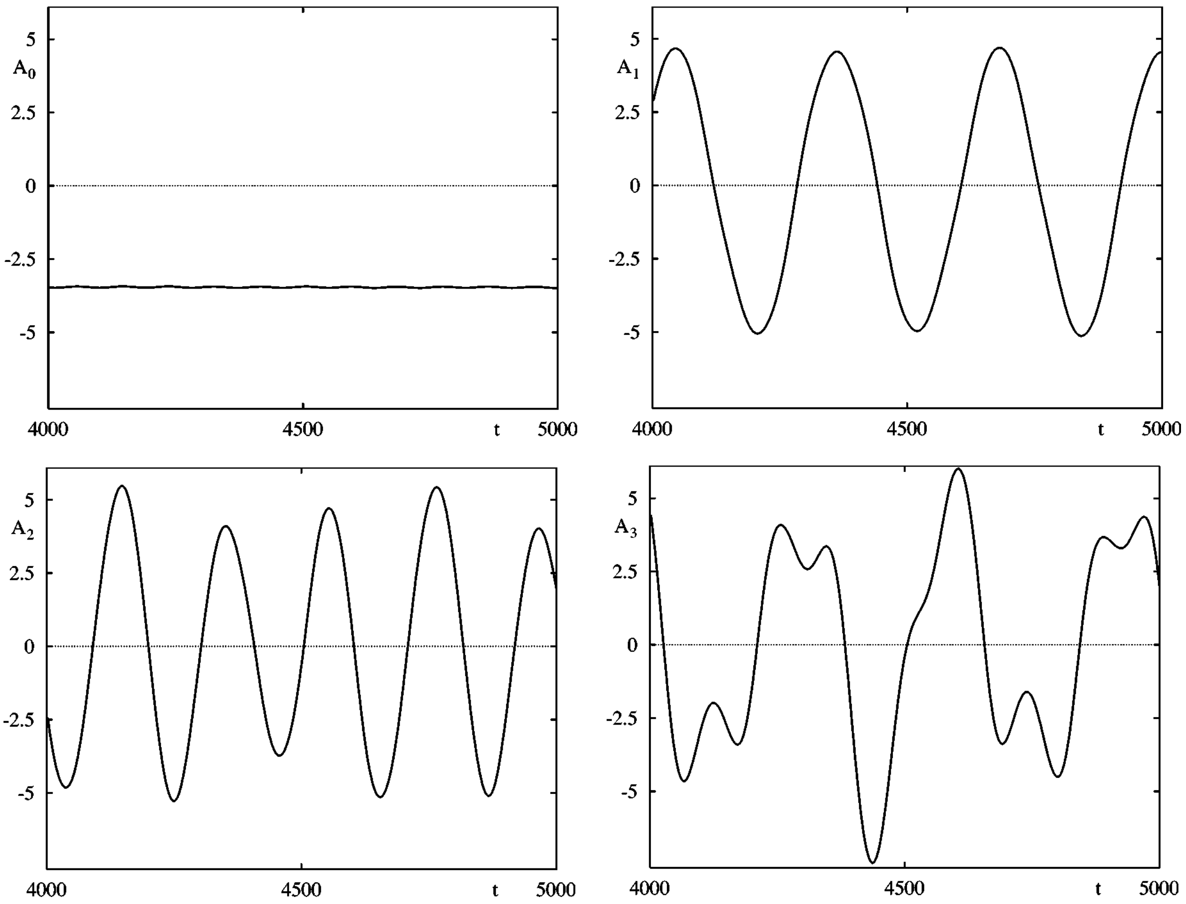

FIG. 7. Temporal behavior of the first four POD modes.

$$\frac{\partial}{\partial t}\begin{pmatrix}\nabla_\perp^2\phi\\ p\end{pmatrix}=\mathbf{L}\begin{pmatrix}\phi\\ p\end{pmatrix}+\left\{\phi,\begin{pmatrix}\nabla_\perp^2\phi\\ p\end{pmatrix}\right\}. \tag{11}$$

We construct a one-field equation that captures the main features of Eq. (11), i.e., the same linear stability and the same nonlinearity for the potential

$$\frac{\partial}{\partial t}\nabla_\perp^2\phi=\mathbf{L}_{\text{eff}}\phi+\{\phi,\nabla_\perp^2\phi\}, \tag{12}$$

where the linear operator $\mathbf{L}_{\text{eff}}$ is such that its eigenvalues are those of the operator $\mathbf{L}$ in Eq. (11) and the eigenvectors are close to the global modes. We approximate these modes by

$$\phi_0=B_0F(x),$$

$$\phi_1=B_1\sum_\mu F(x)F_\mu(x)\exp i[(m_0+\mu)\theta-n\varphi]+\text{c.c.},$$

$$\phi_{\bar{1}}=iB_{\bar{1}}\sum_\mu xF(x)F_\mu(x)\exp i[(m_0+\mu)\theta-n\varphi]+\text{c.c.},$$

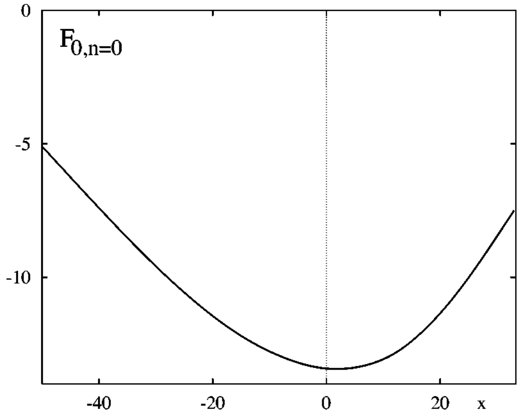

FIG. 8. Radial dependence of the dominant $(m,n)=(0,0)$ part of the most important POD mode.

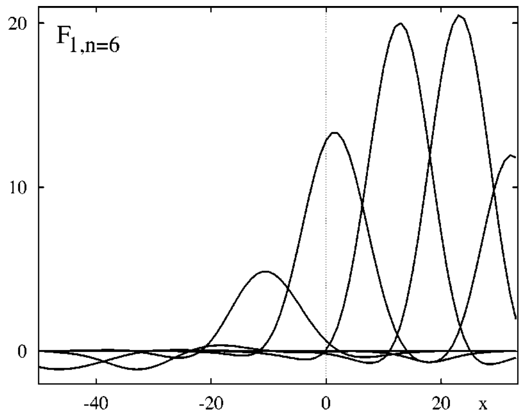

FIG. 9. Radial profile of Fourier modes involved in the dominant $n=6$ part of the second most important POD mode.

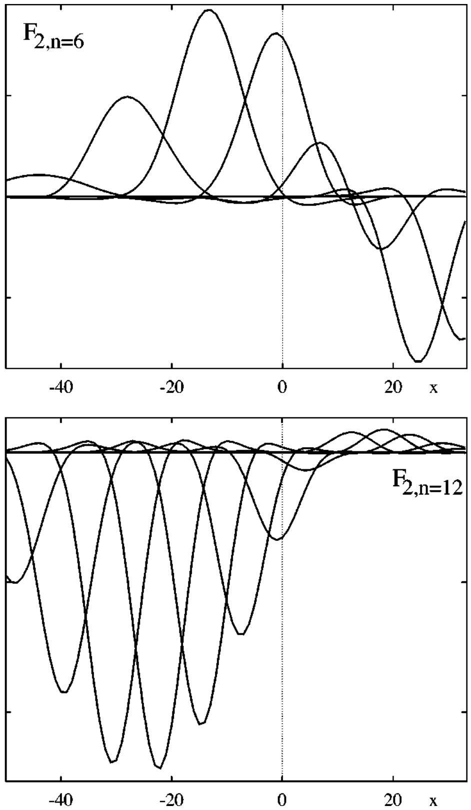

FIG. 10. Radial structures of the dominant $n=6$ (a) and $n=12$ (b) parts for the third most important POD mode.

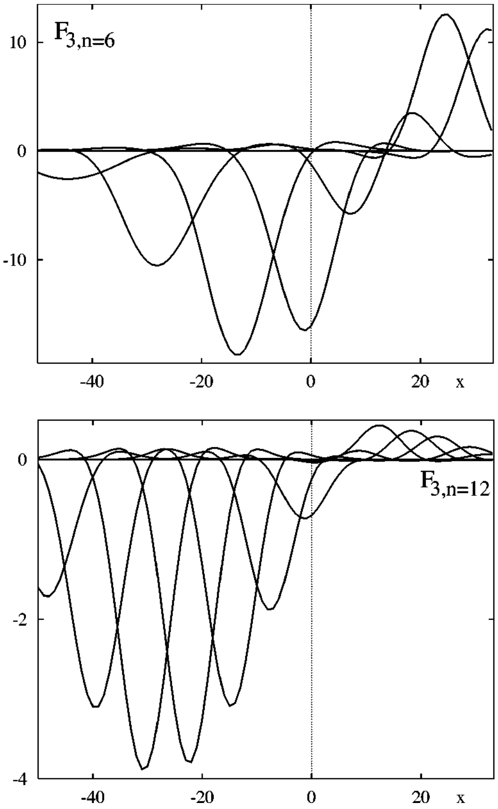

FIG. 11. Same as Fig. 10, for the fourth most important POD mode.

$$\phi_2=B_2\sum_{\mu} F(x)F_{\mu}(x)\exp 2i[(m_0+\mu)\theta-n\varphi]+\text{c.c.},$$

$$\phi_{\bar{2}}=iB_{\bar{2}}\sum_{\mu} xF(x)F_{\mu}(x)\exp 2i[(m_0+\mu)\theta-n\varphi]+\text{c.c.},$$

where

$$F(x)=\exp\left(-\frac{x^2}{2L^2}\right),\quad F_{\mu}(x)=\exp\left[-\frac{(x-\mu d)^2}{2w^2}\right]$$

and

$$B_0^2=\frac{1}{\sqrt{2\pi}L},\quad B_1^2=B_2^2=\frac{d}{2\pi Lw},\quad B_{\bar{1}}^2=B_{\bar{2}}^2=\frac{d}{\pi L^3 w}.$$

Here, w represents the radial width of the Fourier modes involved in the global modes and L is the width of the envelope. The normalization is such that $\langle\phi_i,\phi_j\rangle=\delta_{ij}$ with the standard scalar product.

Using the Galerkin approximation

$$\phi=a_0\phi_0+a_1\phi_1+a_{\bar{1}}\phi_{\bar{1}}+a_2\phi_2+a_{\bar{2}}\phi_{\bar{2}}$$

in the evolution equation (12) and multiplying by each of the modes ϕ_i reveals the amplitude equations

$$\dot{a}_0=\gamma_0 a_0+C_0^{1\bar{1}}a_1 a_{\bar{1}}+C_0^{2\bar{2}}a_2 a_{\bar{2}},\tag{13a}$$

$$\dot{a}_1=\gamma_1 a_1+C_1^{0\bar{1}}a_0 a_{\bar{1}}+C_1^{\bar{1}2}a_{\bar{1}}a_2+C_1^{1\bar{2}}a_1 a_{\bar{2}},\tag{13b}$$

$$\dot{a}_{\bar{1}}=\gamma_{\bar{1}}a_{\bar{1}}+C_{\bar{1}}^{01}a_0 a_1+C_{\bar{1}}^{12}a_1 a_2+C_{\bar{1}}^{\overline{12}}a_{\bar{1}}a_{\bar{2}},\tag{13c}$$

$$\dot{a}_2=\gamma_2 a_2+C_2^{0\bar{2}}a_0 a_{\bar{2}}+C_2^{1\bar{1}}a_1 a_{\bar{1}},\tag{13d}$$

$$\dot{a}_{\bar{2}}=\gamma_{\bar{2}}a_{\bar{2}}+C_{\bar{2}}^{02}a_0 a_2+C_{\bar{2}}^{11}a_1^2+C_{\bar{2}}^{\overline{11}}a_{\bar{1}}^2,\tag{13e}$$

where the coefficients are given by

$$C_i^{jk}=\alpha_{jk}\langle\phi_i,\{\phi_j,\nabla_{\perp}^2\phi_k\}+\{\phi_k,\nabla_{\perp}^2\phi_j\}\rangle$$

and $\alpha_{jk}=1-\delta_{jk}/2$. Note that we only specify the nonzero coefficients; other coefficients are vanishing due to symmetry. The only nonvanishing coefficients in the evolution equation for a_0 that correspond to the amplitude of the shear flow are $C_0^{1\bar{1}}$ and $C_0^{2\bar{2}}$. This means that the only effective coupling for shear flow generation is given by the interaction of the most unstable global mode with the *second* most unstable global mode with the same toroidal wave number n. Therefore, we expect the shear flow generation to set in clearly above the instability threshold, when the second most unstable global mode is only weakly damped. This is in agreement with the numerical simulations shown in Figs. 4 and 5 and was also found in the detailed analysis of shear flow generation in 2D interchange turbulence in Ref. [9].

Calculating the coefficients leads to

$$C_0^{1\bar{1}}=\frac{4w^2}{L^2}\tilde{D},$$

$$C_0^{2\bar{2}}=2C_0^{1\bar{1}},$$

$$C_1^{0\bar{1}}=-\left[1+6\frac{L^2w^2}{r_0^2d^2}\left(1+\frac{w^2}{2L^2}+\frac{m_0^2d^2}{3L^2}\right)\right]\tilde{D},$$

$$C_1^{\bar{1}2}=\left[1+\frac{w^2}{L^2}-\frac{9}{2}\,\frac{L^2w^2}{r_0^2d^2}\left(1+\frac{w^2}{L^2}+\frac{m_0^2d^2}{L^2}\right)\right]D,$$

$$C_1^{1\bar{2}}=\left(1+\frac{w^2}{L^2}\right)D,$$

$$C_{\bar{1}}^{01}=\left[1-\frac{4w^2}{L^2}+6\frac{L^2w^2}{r_0^2d^2}\left(1+\frac{w^2}{2L^2}+\frac{m_0^2d^2}{3L^2}\right)\right]\tilde{D},$$

$$C_{\bar{1}}^{12}=\left[1+\frac{w^2}{L^2}+\frac{9}{2}\,\frac{L^2w^2}{r_0^2d^2}\left(1+\frac{w^2}{L^2}+\frac{m_0^2d^2}{L^2}\right)\right]D,$$

$$C_{\bar{1}}^{\bar{1}\bar{2}}=-2\frac{w^2}{L^2}D,$$

$$C_2^{0\bar{2}}=2C_1^{0\bar{1}},$$

$$C_2^{1\bar{1}}=-2\left(1+\frac{w^2}{L^2}\right)D,$$

$$C_{\bar{2}}^{02}=2C_{\bar{1}}^{01},$$

$$C_{\bar{2}}^{11}=-C_1^{1\bar{2}},$$

$$C_{\bar{2}}^{\bar{1}\bar{1}}=2\frac{w^2}{L^2}D,$$

where

$$D=\frac{4m_0d^{1/2}}{9\pi^{1/2}r_0L^{3/2}w^{5/2}},\qquad \tilde{D}=\frac{3^{1/2}\pi^{1/4}w^{1/2}}{2^{9/4}d^{1/2}}D.$$

Note that the energy conservation of the quadratic nonlinearity is verified by

$$C_0^{1\bar{1}}+C_1^{0\bar{1}}+C_{\bar{1}}^{01}=0,$$

$$C_0^{2\bar{2}}+C_2^{0\bar{2}}+C_{\bar{2}}^{02}=0,$$

$$C_1^{\bar{1}2}+C_{\bar{1}}^{12}+C_2^{1\bar{1}}=0,$$

$$C_1^{1\bar{2}}+C_{\bar{2}}^{11}=0,$$

$$C_{\bar{1}}^{\bar{1}\bar{2}}+C_{\bar{2}}^{\bar{1}\bar{1}}=0.$$

As we have seen, the POD of the fluctuating data from the numerical simulation reveals that the weights of the modes are strongly decreasing with increasing weight number. We therefore apply the following scaling to the amplitudes:

$$a_0,a_1,a_{\bar{1}}\sim\epsilon,\qquad a_2,a_{\bar{2}}\sim\epsilon^2.$$

Additionally, we use an argument usually applied in (generalized) center manifold reductions [9] which states that the dynamics of the stable modes is governed by the dominating modes, i.e., the first are ‘‘slaved’’ by the latter. In order to further simplify the amplitude equations (13), we assume that modes 2 and $\bar{2}$ play the role of the slaved modes providing an energy sink. Accordingly, γ_2 and $\gamma_{\bar{2}}$ are negative and the amplitudes $a_2,a_{\bar{2}}$ are functions of $a_0,a_1,a_{\bar{1}}$. Assuming that the slaved modes relax rapidly to the amplitudes determined by the dominating modes, we can calculate this functional dependence from (13d, 13e) by setting the time derivatives to zero and solving for a_2 and $a_{\bar{2}}$, respectively. Setting $\epsilon=w^2/L^2\sim L^2/r_0^2$, the result is

$$a_2=-2\frac{D}{|\gamma_2|}a_1a_{\bar{1}}+O(\epsilon^3),$$

$$a_{\bar{2}}=-\frac{D}{|\gamma_{\bar{2}}|}a_1^2+O(\epsilon^3).$$

Using these expressions in (13a–13c), we obtain a simplified system of amplitude equations (neglecting terms of order ϵ^4)

$$\dot{\tilde{a}}_0=-\epsilon\tilde{\gamma}_0\tilde{a}_0+\epsilon\tilde{\gamma}_0\tilde{a}_1\tilde{a}_{\bar{1}},\tag{14a}$$

$$\dot{\tilde{a}}_1=\gamma_1\tilde{a}_1-\tilde{a}_0\tilde{a}_{\bar{1}}-\nu_1\tilde{a}_{\bar{1}}^2\tilde{a}_1-\nu_2\tilde{a}_1^3,\tag{14b}$$

$$\dot{\tilde{a}}_{\bar{1}}=-\tilde{\gamma}_{\bar{1}}\tilde{a}_{\bar{1}}+\tilde{a}_0\tilde{a}_1-\nu_1\tilde{a}_1^2\tilde{a}_{\bar{1}},\tag{14c}$$

where

$$\epsilon\tilde{\gamma}_0=-\gamma_0>0,\qquad \tilde{\gamma}_{\bar{1}}=-\gamma_{\bar{1}}>0,$$

$$\nu_1=\frac{D^2}{\tilde{D}^2}\,\frac{\tilde{\gamma}_0}{|\gamma_2|},\qquad \nu_2=\frac{D^2}{2\tilde{D}^2}\,\frac{\tilde{\gamma}_0}{|\gamma_{\bar{2}}|},$$

and

$$\tilde{a}_0=\tilde{D}a_0,\qquad \tilde{a}_1=\frac{2\tilde{D}}{\sqrt{\tilde{\gamma}_0}}a_1,\qquad \tilde{a}_{\bar{1}}=\frac{2\tilde{D}}{\sqrt{\tilde{\gamma}_0}}a_{\bar{1}}.$$

The system (14) has two nontrivial fixed points. The first one, for which there is no shear flow, is given by

$$\tilde{a}_0=0,\qquad \tilde{a}_1^2=\frac{\gamma_1}{\nu_2},\qquad \tilde{a}_{\bar{1}}=0.$$

It corresponds to the *L* state. For a low enough dissipation, so that

$$\frac{\gamma_1}{\nu_2}>\frac{\tilde{\gamma}_{\bar{1}}}{1-\nu_1}>0,\tag{15}$$

this state is unstable and the system evolves to a second fixed point with nonvanishing shear flow and reduced fluctuation level (*H* state),

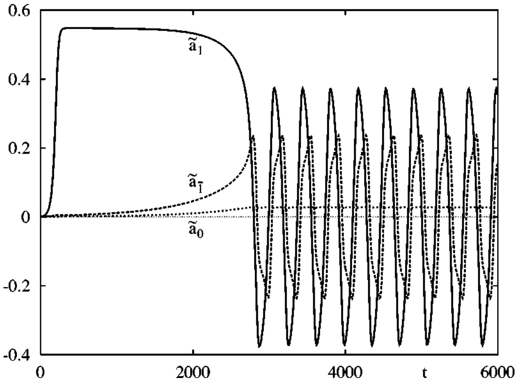

FIG. 12. Typical solution of the low-dimensional system (14). The parameters are $\gamma_0=-0.001$, $\gamma_1=0.03$, $\gamma_{\bar{1}}=-0.005$, $\nu_1=4\nu_2$, and $\nu_2=0.1$.

$$\tilde{a}_0=\tilde{a}_1\tilde{a}_{\bar{1}},\qquad \tilde{a}_1^2=\frac{\tilde{\gamma}_{\bar{1}}}{1-\nu_1},$$

$$\tilde{a}_{\bar{1}}^2=\frac{\nu_2}{1+\nu_1}\left(\frac{\gamma_1}{\nu_2}-\frac{\tilde{\gamma}_{\bar{1}}}{1-\nu_1}\right).$$

Considering the linear stability problem of this fixed point, the leading terms of the eigenvalues can be easily calculated (two of them are of order one, the third is of order ϵ). The result is that the H state becomes unstable for

$$\frac{2\nu_1^2}{1+\nu_1}\left(\frac{\gamma_1}{\nu_2}-\frac{\tilde{\gamma}_1}{1-\nu_1}\right)>\frac{\tilde{\gamma}_{\bar{1}}}{1-\nu_1}.$$

It can be shown that due to the presence of the dissipative terms, the solutions of the system (14) are bounded. The Poincaré-Bendixson theorem (for details see, e.g., [16]) then implies that in the case where the two fixed points are unstable, the amplitudes evolve to a limit cycle, i.e., the system shows an oscillatory behavior.

For a typical set of parameters, $\gamma_1/\tilde{\gamma}_{\bar{1}}=6$ and $\gamma_2/\tilde{\gamma}_{\bar{2}}=2\nu_2/\nu_1=1/2$, the following scenario appears when lowering the control parameter ν_2: The L state becomes unstable at $\nu_2=0.24$. Below this threshold, the system evolves to the H state. The latter is stable up to $\nu_2=(47+7\sqrt{41})/400\approx 0.2296$. For lower values of the dissipation, oscillating solutions are observed. A typical example is shown in Fig. 12. This bifurcation behavior is in agreement with the observations in the numerical simulations of the full dynamical system.

Note that if we assume that the mode $\bar{1}$ is slaved (instead of dominating) and of the order ϵ^2 (instead of ϵ), a simplified system of equations for the amplitudes $\tilde{a}_0$ and $\tilde{a}_1$ can be constructed in the same way as presented above. This system is close to the one obtained in Ref. [4] by a statistical analysis in the case of strongly developed turbulence which was presented as a paradigm for low to high (L-H) confinement transition. However, this system does not reproduce the instability of the H state and the evolution to oscillating states.

IV. CONCLUSION

In this paper we applied a synergetic method to study nonlinear dynamical systems close to a stability threshold. It consists of a combination of a POD and a subsequent Galerkin projection. The POD reveals the relevant modes in the dynamical process considered, while the Galerkin projection provides a corresponding low-dimensional model. We illustrated the method using the process of shear flow generation in a 3D plasma dynamical system. The method can in principle be used to investigate a large family of models. Indeed, the dynamical system describing resistive ballooning fluctuations in a tokamak belongs to a large class of convective fluid systems including Rayleigh-Bénard convection.

Numerical simulations were performed and a POD of the fluctuating signal showed that there is a small number of relevant modes. These modes are close to the linear modes. This is not a trivial result because the linear eigenmodes have a large radial extent (global modes) and are therefore expected to be modified by the nonlinear coupling. The low-dimensional model deduced by a Galerkin projection governs the main features of shear flow generation, turbulence reduction (L-H transition), and the existence of oscillating solutions. It reproduces qualitatively the main properties of the full numerical simulations.

APPENDIX

Here we present the calculation of the linear eigenmodes including the first order in the ballooning approximation. The operators $\mathbf{L}_1$ and $\mathbf{L}_2$ appearing in the eigenvalue problem (8) are given by

$$\mathbf{L}_1=\frac{2}{m_0 s_0^2}\begin{pmatrix}\frac{1}{k_\perp^2} & 0\\ 0 & \chi_\parallel\end{pmatrix}\frac{\partial^2}{\partial\theta'^2}\frac{\partial}{\partial\theta_0}+\frac{1}{m_0}\begin{pmatrix}\frac{2(m_0\kappa_y)^2}{k_\perp^2}(\gamma+2\nu k_\perp^2) & -\frac{m_0\kappa_y\cos(\theta')}{k_\perp^2}\\ -m_0\kappa_y & 2(m_0\kappa_y)^2\chi_\perp\end{pmatrix}\left(\frac{\partial}{\partial\theta'}+\frac{\partial}{\partial\theta_0}\right),$$

$$\mathbf{L}_2=\frac{1}{m_0^2}\begin{pmatrix}\frac{(m_0\kappa_y)^2}{k_\perp^2}\{\gamma+2\nu[k_\perp^2+2(m_0\kappa_y)^2]\} & 0\\ 0 & (m_0\kappa_y)^2\chi_\perp\end{pmatrix}\left(\frac{\partial}{\partial\theta'}+\frac{\partial}{\partial\theta_0}\right)^2.$$

Note that $|\phi/p| \sim \epsilon$, $\nu, \chi_\perp \sim \epsilon^2$, and for consistency with the linear approximation in the safety factor, the contributions of the second and higher order in $(R_0 \xi q_0 x)/(r_0 L_s) = x/(m_0 d_0)$ have been neglected in the parallel gradient. The lowest order problem (6) is represented by $\mathbf{L}_0 \Phi_0(\theta', \theta_0) = 0$. The most unstable solution $\tilde{\Phi}_0(\theta', 0)$ turns out to be an even function of θ'. Additionally, Eq. (8) implies that its solution has the same parity in θ' and θ_0. Therefore, separating a slowly varying (in $\theta_0 = \epsilon^{1/2} \tilde{\theta}_0$) amplitude and developing the remaining factor in a series around $\theta_0 = 0$, the lowest order solution can be written as

$$\tilde{\Phi}_0(\theta', \theta_0) = A(\tilde{\theta}_0) \left(\tilde{\Phi}_0(\theta', 0) + \frac{\epsilon}{2} \frac{\partial^2 \tilde{\Phi}_0}{\partial \theta_0^2} \bigg|_0 \tilde{\theta}_0^2 \right).$$

Developing the growth rate $\gamma_0(\theta_0)$ and the operator $\mathbf{L}_0(\gamma, \theta', \theta_0)$ around $\theta_0 = 0$, the lowest order equation becomes

$$\epsilon^{1/2} \frac{\partial \mathbf{L}_0}{\partial \theta_0} \Big|_0 \tilde{\Phi}_0(\theta', 0) \tilde{\theta}_0 + \frac{\epsilon}{2} \left[\mathbf{L}_0(\gamma_0(0), \theta', 0) \frac{\partial^2 \tilde{\Phi}_0}{\partial \theta_0^2} \bigg|_0 + \left(\frac{\partial \mathbf{L}_0}{\partial \gamma} \bigg|_{\gamma_0(0)} \frac{d^2 \gamma_0}{d \theta_0^2} \bigg|_0 + \frac{\partial^2 \mathbf{L}_0}{\partial \theta_0^2} \bigg|_0 \right) \tilde{\Phi}_0(\theta', 0) \right] \tilde{\theta}_0^2 = 0. \tag{A1}$$

We now look for a solution of the two-dimensional eigenvalue problem (8) in the vicinity of $\tilde{\Phi}_0(\theta', \theta_0)$ and $\gamma_0(0)$,

$$\Phi(\theta', \theta_0) = \tilde{\Phi}_0(\theta', \theta_0) + \epsilon^{1/2} \Phi_1(\theta', \theta_0) + \epsilon \Phi_2(\theta', \theta_0),$$

$$\gamma = \gamma_0(0) + \epsilon^{1/2} \tilde{\gamma}_1 + \epsilon \tilde{\gamma}_2.$$

Developing Eq. (8) and using Eq. (A1), we find

$$\mathbf{L}_0(\gamma_0(0), \theta', 0)(\epsilon^{1/2} \Phi_1 + \epsilon \Phi_2) + \left\{ \left[\epsilon^{1/2} \tilde{\gamma}_1 + \epsilon \left(\tilde{\gamma}_2 - \frac{1}{2} \frac{d^2 \gamma_0}{d \theta_0^2} \bigg|_0 \tilde{\theta}_0^2 \right) \right] \frac{\partial \mathbf{L}_0}{\partial \gamma} \bigg|_{\gamma_0(0)} + i \epsilon \mathbf{L}_1 + i \epsilon^{3/2} \tilde{\gamma}_1 \frac{\partial \mathbf{L}_1}{\partial \gamma} \bigg|_{\gamma_0(0)} + \epsilon^2 \mathbf{L}_2 \right\} A(\tilde{\theta}_0) \tilde{\Phi}_0(\theta', 0) + O(\epsilon^{3/2}) = 0,$$

where we have assumed even parity for Φ_1 and Φ_2 as for $\tilde{\Phi}_0$. Multiplying by the adjoined function $\tilde{\Phi}_0^+(\theta', 0)$ and integrating in θ' yields at orders $\epsilon^{1/2}$ and ϵ the solvability conditions

$$\tilde{\gamma}_1 C_0 A + i C_1 \frac{dA}{d \tilde{\theta}_0} = 0, \tag{A2}$$

$$\left(\tilde{\gamma}_2 - \frac{1}{2} \frac{d^2 \gamma_0}{d \theta_0^2} \bigg|_0 \tilde{\theta}_0^2 \right) C_0 A + C_2 \frac{d^2 A}{d \tilde{\theta}_0^2} = 0, \tag{A3}$$

where

$$C_0 = \int_{-\infty}^{\infty} d\theta' (\tilde{\phi}_0^+ \tilde{\phi}_0 + \tilde{p}_0^+ \tilde{p}_0),$$

$$C_1 = \frac{1}{m_0} \int_{-\infty}^{\infty} d\theta' \left\{ -\frac{2(m_0 \kappa_y)^2}{k_\perp^2} \tilde{\phi}_0^+ \left[\gamma_0(0) + d_0^2 \frac{\partial^2}{\partial \theta'^2} + 2 \nu k_\perp^2 \right] \tilde{\phi}_0 + i m_0 \kappa_y \left[\frac{\cos(\theta')}{k_\perp^2} \tilde{\phi}_0^+ \tilde{p}_0 - \tilde{p}_0^+ \tilde{\phi}_0 \right] - 2(m_0 \kappa_y)^2 \tilde{p}_0^+ \left(\chi_\parallel d_0^2 \frac{\partial^2}{\partial \theta'^2} + \chi_\perp \right) \tilde{p}_0 \right\},$$

$$C_2 = -\frac{1}{m_0^2} \int_{-\infty}^{\infty} d\theta' \left[\frac{(m_0 \kappa_y)^2}{k_\perp^2} \tilde{\phi}_0^+ \{ \gamma_0(0) + 2 \nu [k_\perp^2 + 2(m_0 \kappa_y)^2] \} \tilde{\phi}_0 + (m_0 \kappa_y)^2 \chi_\perp \tilde{p}_0^+ \tilde{p}_0 \right],$$

where $k_\perp$ has to be evaluated at $\theta_0 = 0$. It turns out that $C_1 \ll C_0$ and therefore from Eq. (A2) $\tilde{\gamma}_1 \approx 0$. This has been used in Eq. (A3). The most unstable solution of the latter is

$$A(\tilde{\theta}_0) = \exp\left(-\frac{\tilde{\alpha}}{2} \tilde{\theta}_0^2 \right),$$

where

$$\tilde{\alpha}^2 = \frac{C_0}{2 C_2} \frac{d^2 \gamma_0}{d \theta_0^2} \bigg|_0, \quad \tilde{\gamma}_2 = \frac{C_2}{C_0} \tilde{\alpha}.$$

A solution of Eq. (8) which is periodic in $\theta' = \theta$ can be constructed,

$$\Phi(\theta', \theta_0) = \exp\left(-\frac{\alpha}{2} \theta_0^2 \right) \sum_{l=-\infty}^{\infty} \tilde{\Phi}_0(\theta' - 2\pi l, 0),$$

where $\alpha = \tilde{\alpha}/\epsilon$. The back-transformation of Eqs. (3)–(5) for $y \in [-\pi/\kappa_y; \pi/\kappa_y]$ gives the result (9) presented in the main part of the paper.

---

[1] J. L. Lumley, in *Atmospheric Turbulence and Radio Wave Propagation*, edited by A. M. Yaglom and V. I. Tatarski (Nauka, Moscow, 1967), p. 166.

[2] G. Berkooz, P. Holmes, and J. Lumley, Annu. Rev. Fluid Mech. **25**, 539 (1993).

[3] M. C. Cross and P. C. Hohenberg, Rev. Mod. Phys. **65**, 151 (1993).

[4] P. H. Diamond, Y.-M. Liang, B. A. Carreras, and P. W. Terry, Phys. Rev. Lett. **72**, 2565 (1994).

[5] R. J. Groebner, Phys. Fluids B **5**, 2343 (1993).

[6] J. W. Connor, J. B. Taylor, and H. R. Wilson, Phys. Rev. Lett. **70**, 1803 (1993).
[7] F. Romanelli and F. Zonca, Phys. Fluids B **5**, 4081 (1993).
[8] J. Y. Kim and M. Wakatani, Phys. Rev. Lett. **73**, 2200 (1994).
[9] P. Beyer and K. H. Spatschek, Phys. Plasmas **3**, 995 (1996).
[10] B. Scott, Plasma Phys. Controlled Fusion **39**, 471 (1997).
[11] A. Zeiler, D. Biskamp, J. F. Drake, and P. N. Guzdar, Phys. Plasmas **3**, 2951 (1996).
[12] P. Beyer, X. Garbet, and P. Ghendrih, Phys. Plasmas **5**, 4271 (1998).
[13] X. Garbet, Y. Sarazin, P. Beyer, P. Ghendrih, R. Waltz, M. Ottaviani, and S. Benkadda, Nucl. Fusion **39**, 2063 (1999).
[14] Y. Sarazin, P. Ghendrih, and X. Garbet, Phys. Plasmas **5**, 4214 (1998).
[15] S. Benkadda, T. Dudok de Wit, A. Verga, A. Sen, ASDEX Team, and X. Garbet, Phys. Rev. Lett. **73**, 3403 (1994).
[16] J. D. Murray, *Mathematical Biology* (Springer, Berlin, 1989).